SCIENTIFIC REPORTS

OPEN

Elasticity of Ferropericlase across the Spin Crossover in the Earth's Lower Mantle

Jing Yang[1], Xinyue Tong[1], Jung-Fu Lin[1,2], Takuo Okuchi[3] & Naotaka Tomioka[3]

Knowing the elasticity of ferropericlase across the spin transition can help explain seismic and mineralogical models of the lower-mantle including the origin of seismic heterogeneities in the middle to lowermost parts of the lower mantle[1–4]. However, the effects of spin transition on full elastic constants of ferropericlase remain experimentally controversial due to technical challenges in directly measuring sound velocities under lower-mantle conditions[1–5]. Here we have reliably measured both V_P and V_S of a single-crystal ferropericlase (($Mg_{0.92}$,$Fe_{0.08}$)O) using complementary Brillouin Light Scattering and Impulsive Stimulated Light Scattering coupled with a diamond anvil cell up to 96 GPa. The derived elastic constants show drastically softened C_{11} and C_{12} within the spin transition at 40–60 GPa while C_{44} is not affected. The spin transition is associated with a significant reduction of the aggregate V_P/V_S via the aggregate V_P softening because V_S softening does not visibly occur within the transition. Based on thermoelastic modelling along an expected geotherm, the spin crossover in ferropericlase can contribute to 2% reduction in V_P/V_S in a pyrolite mineralogical model in mid lower-mantle. Our results imply that the middle to lowermost parts of the lower-mantle would exhibit enhanced seismic heterogeneities due to the occurrence of the mixed-spin and low-spin ferropericlase.

Seismic wave studies of the lower mantle have established relatively reliable seismic models including compressional and shear wave velocities (V_P and V_S) in one-, two-, and three-dimensional tomographic models (e.g., PREM, AK135, S40RTS)[6–8]. Thus far, it has been shown that most of the lower mantle, except the lowermost mantle such as the D′′ layer, exhibit relatively smooth changes in seismic parameters that have been commonly interpreted as a result of the high pressure-temperature (*P-T*) effects on physical properties of candidate minerals in the region. The lower mantle is mostly believed to be seismically and chemically homogeneous and likely consisting of approximately 75% bridgmanite (silicate perovskite (Mg,Fe)(Al,Fe,Si)O_3; Pv), 20% ferropericlase ((Mg,Fe)O; Fp), and 5% calcium perovskite (CaSiO$_3$) by volume in a pyrolite compositional model[9,10]. However, a number of seismic studies have shown that possible thermal and/or chemical heterogeneities, especially in the middle to lower part of the lower mantle ranging from approximately 1500 km to 2800 km in depth, are needed to reconcile differences between our current understanding of seismic models and mineral physics results[11–15]. Other than the bridgmanite to post-perovskite structural transition at the D′′ zone region[16], which may be responsible for the seismic discontinuities in the lowermost mantle, the electronic spin transitions of iron in lower-mantle minerals have been suggested to affect our understanding of mid to lowermost lower-mantle seismic heterogeneities.

The electronic spin transition of iron in lower-mantle bridgmanite and ferropericlase has been recently reported to affect physical and chemical properties of the host minerals, including changes in elasticity, iron partitioning, and electrical and thermal conductivities[1,4,17–22], that may contribute to

[1]Department of Geological Sciences, Jackson School of Geosciences, The University of Texas at Austin, Austin, TX 78712, USA. [2]Center for High Pressure Science and Technology Advanced Research (HPSTAR). [3]Institute for Study of the Earth's Interior, 827 Yamada, Misasa, Tottori, 682-0193 Japan. Correspondence and requests for materials should be addressed to J.F.L. (email: afu@jsg.utexas.edu)

seismic heterogeneities of the region. It has been shown that a broad spin crossover occurs in ferropericlase at conditions ranging from 1700 km to 2700 km in depth[23], while the Fe^{3+} in the octahedral site of bridgmanite undergoes a high-spin to low-spin transition at *P-T* conditions relevant to the top lower mantle[5]. Of particular interest to our understanding of deep-mantle seismology and geodynamics are the effects of the spin transition on the elasticity (e.g., sound velocities, equation of states (EoS), and seismic anisotropies) of lower-mantle minerals, because a thorough knowledge of their elastic properties is essential for interpreting seismic observations as well as for constraining the chemical composition and mineralogy of the region[14].

In recent years, there have been a number of experimental and theoretical studies on the elasticity of single-crystal ferropericlase across the spin transition at high pressures using various techniques, including Impulsive Stimulated Light Scattering (ISS), Brillouin Light Scattering (BLS), Inelastic X-ray Scattering (IXS), and Density Function Theory (DFT)[1,3,4,24,25]. DFT calculations have shown that ferropericlase exhibits significant softening in V_P as well as in the C_{11} and C_{12} elastic constants across the spin crossover at lower-mantle *P-T* conditions, although V_S and C_{44} are not affected by the transition[25]. On the other hand, experimental results on the elasticity across the spin transition differ drastically[1–4]. In particular, ISS measurements on $(Mg_{0.94}Fe_{0.06})O$ up to 60 GPa showed a remarkable reduction in both V_P and V_S across the spin transition[1], although the reliability of deriving the V_S from the interfacial wave has been questioned. BLS measurements on $(Mg_{0.9}Fe_{0.1})O$ up to 81 GPa showed no substantial reduction of the directly-measured V_S across the spin transition, while the combination of the V_S values from BLS and the EoS parameters from X-ray diffraction have shown a V_P softening up to 17% within the spin transition[2]. High-pressure IXS experiments up to 80 GPa on $(Mg_{0.83}Fe_{0.17})O$, which used acoustic phonon dispersions at very high frequencies to extract the velocities, did not reveal any reduction of either V_P or V_S within the spin transition[3]. Furthermore, some of these previous studies have indicated that the spin transition can markedly enhance the elastic V_S splitting anisotropy of ferropericlase such that the low-spin state becomes much more elastically anisotropic as compared to its high-spin counterpart[3,4]. The full elastic constants of single-crystal ferropericlase across the spin transition and in the low-spin state can help provide new insight into the effects of the spin transition on thermodynamic and seismic parameters of the sample, but these essential experimental data remain unclear due to the aforementioned technical difficulties. Since different experimental results point to entirely different scenarios for seismic and geochemical models of the lower mantle, seismically homogeneous vs. heterogeneous lower mantle, it remains unclear if the effect of the spin transition on the elasticity of the lower-mantle ferropericlase should be taken into account in our understanding of the seismic models of the lower mantle. Reliable experimental results can also help elucidate recent theoretical predictions of the elasticity and thermodynamics of ferropericlase at high pressures[25].

Here we have directly measured V_P, V_S, and the pressure-volume (*P-V*) relation of a single-crystal ferropericlase $(Mg_{0.92},Fe_{0.08})O$ in order to solve for its full elastic constants (C_{ij}) using combined BLS, ISS, and X-ray diffraction (XRD) measurements in a diamond anvil cell (DAC) up to 96 GPa (see Methods for details). The combined experimental results overcome previous technical difficulties and permit direct and reliable evaluation of the full elastic constants and thermoelastic parameters across the spin transition at lower-mantle pressures. Our results show that ferropericlase with 8 at% iron undergoes a spin transition at 40–60 GPa that is associated with changes in elastic constants: C_{11} softening by a maximum of 16%, and C_{12} by 70%, whereas C_{44} does not show any observable reduction across the transition. Within the spin transition, the aggregate *Ks* and V_P calculated from Voigt-Reuss-Hill average of the elastic constants reduces by 38% and 13%, respectively, and the aggregate V_S is not visibly affected by the spin transition. The V_P anisotropy changes to a maximum value of 11%($\pm$0.7) at 50 GPa, which is midway between the spin transition as compared to 9%($\pm$0.2%) in the V_P anisotropy for the extrapolated high-spin state. The low-spin state also exhibits some elastic behavior distinct from that of the high-spin and mixed-spin states. To decipher the geophysical and geochemical consequences of the spin crossover in the deep mantle, we have modelled elastic and seismic parameters of ferropericlase along an expected lower-mantle geotherm[26]. Our results show that the velocity abnormalities and elastic softening remain significantly strong across the spin crossover in the lower mantle and that the low-spin ferropericlase exhibits significantly enhanced V_P and V_S profiles from that of the extrapolated high-spin state. These results are applied to understand potential seismic and/or chemical heterogeneities induced by the spin transition in the deep lower mantle.

Results and Discussion

Experiments and Thermoelastic Modelling.   *P-V* relations of single-crystal ferropericlase $((Mg_{0.92}, Fe_{0.08})O)$ in the (100) platelet were measured using synchrotron X-ray diffraction up to 91 GPa at room temperature in a DAC. These results are used to evaluate the EoS parameters, the width of the spin transition, and the fraction of the high-spin (HS) and low-spin (LS) states in ferropericlase[20,23] (Fig. S1 and Fig. S2) (See Methods and SI for details of the experiments and modelling). Analysis of the measured *P-V* curve shows that the spin transition occurs over pressures ranging between 40 GPa and 60 GPa, and is associated with a density increase of 1.2% (0.1%). The derived isothermal bulk modulus at ambient conditions (K_{T0}) and its pressure derivative (K_{T0}') are: $K_{T0} = 152.5$ (2.4) and $K_{T0}' = 4.1$ (0.2) for the HS state, and $K_{T0} = 161.6$ (7.1) with a fixed K_{T0}' of 4 for the LS state, consistent with previous studies[27] (Fig. S3).
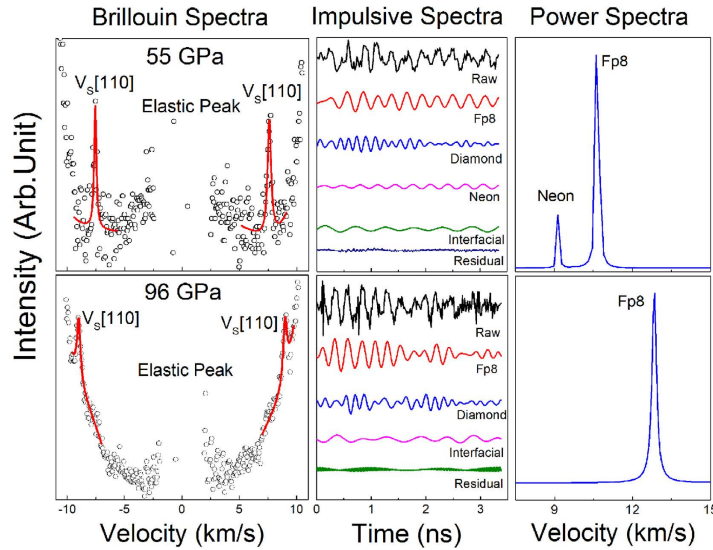
Figure 1. Representative Brillouin light scattering (BLS), impulsive stimulated scattering (ISS), and power spectra of the single-crystal ferropericlase (Mg$_{0.92}$Fe$_{0.08}$)O along [110] crystallographic axis at high pressures. The BLS spectra were used to derive the V_S, while the V_P was detected in the ISS spectra. The ISS spectra in the time domain were analyzed and Fourier-transformed to the power spectra in the velocity (frequency) domain to derive the acoustic waves of the sample at high pressures. Neon medium was also observed in the ISS spectra at pressures up to approximately 70 GPa.

The single-crystal platelet was also used for simultaneously measuring V_S in the BLS experiments and V_P in the ISS experiments along principle [100] and [110] crystallographic axes up to 96 GPa in the Mineral Physics Laboratory of The University of Texas at Austin (Figs 1 and 2); at relatively lower pressures, the V_P and V_S velocities of the platelet were also measured as a function of the azimuthal angles in order to confirm the orientation of the platelets and to further assure the reliability of our measurements as compared with previous studies (Fig. S4). Together with P-V results from XRD measurements, the measured V_P and V_S velocities of single-crystal ferropericlase permit direct derivations of the full elastic constants (C_{11}, C_{12}, C_{44}) at high pressures via Christoffel's equations (Fig. 2). Using the Eulerian finite-strain theory[28] and a thermoelastic model for the cubic system[25], we have modelled the elastic constants within the spin transition using formulations reported previously[25] (See SI for details). Specifically, the elastic compliances S_{ij} of the crystal across the spin transition are given by:

$$S^{ij}V = n_{LS}S^{ij}_{LS}V_{LS} + (1 - n_{LS})S^{ij}_{HS}V_{HS} - \left(\frac{\partial G_{LS}}{\partial \sigma_j} - \frac{\partial G_{HS}}{\partial \sigma_j}\right)\frac{\partial n_{LS}}{\partial \sigma_i},$$

(1)

where V is the volume, n_{LS} is the LS fraction, σ_i and σ_j are the ith and jth stress component, respectively, in the Voigt notation, and G is the Gibbs free energy. In this modelling, the low-spin fraction (n_{LS}) and the unit cell volume (V) derived from the equation of state, and the elastic constants (C_{ij}) are used to constrain the elastic compliances S_{ij} according to the relationship between C_{ij} and S_{ij} (See SI for details). To further obtain the pressure-dependent EoS parameters for the HS and LS states, respectively, the elastic constants and the aggregate bulk and shear moduli as a function of pressure are derived by fitting the results to the third-order Eulerian finite-strain equation of state (Figs 2 and 3).

Examination of the directly-measured V_P and V_S velocities show that the V_P softens by ~10% maximum in both the [100] and [110] directions within the spin transition, while the V_S along the [100] is slightly enhanced, but the V_S along the [110] is not noticeably affected (Fig. 2A) (see SI for comparison with previous results). Furthermore, the C_{11} and C_{12} elastic constants are significantly softened by a maximum of 16% and 70%, respectively, across the spin transition, but C_{44} is not affected by the spin transition (Fig. 2B). The maximum softening for these parameters occurs at approximately 50 GPa, which is midway within the spin transition where the fraction of the LS state is about 50% (Fig. S2). As reported in previous theoretical calculations[25], the C_{11} and C_{12} softening can be explained by the addition of an energy abnormality as a result of the HS and LS mixing (shown in the last term in Equation (1)). Since $n(\sigma_4)$ is an even function and $\partial n/\partial \sigma_4 |_{\sigma_4=0} = 0$, the last term in Equation (1) vanishes such that the C_{44} softening is not expected to occur across the spin crossover[25]. Our results thus confirm theoretical predictions of the elasticity across the spin transition in ferropericlase at high pressures. The derived elastic constants are used to calculate V_{S1}, V_{S2}, and V_P velocities as a function of propagation directions ($\boldsymbol{n}$) by
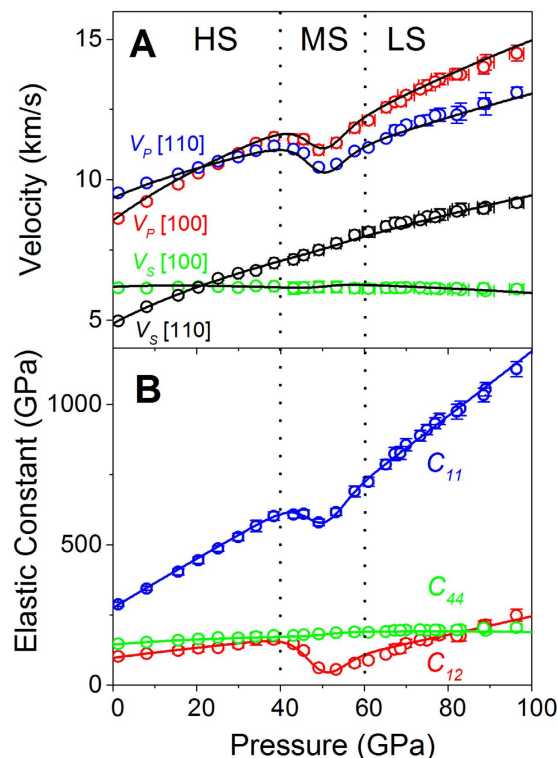
Figure 2. Elasticity of single-crystal ferropericlase (Mg$_{0.92}$Fe$_{0.08}$)O as a function of pressure at 300 K.
(**A**) Compressional and shear wave velocities along the [100] and [110] crystallographic axes as a function of pressure. Compressional wave velocities were measured using the ISS technique, while shear wave velocities were measured using the BLS technique. Open circles: experimental data; solid lines: modelled velocity profiles using thermoelastic equations (see SI for details). (**B**) Elastic constants (C_{ij}) as a function of pressure. Open circles: C_{ij} directly derived from measured compressional and shear wave velocities via Christoffel's equations; solid lines: modelled C_{ij} profiles. Vertical dashed lines are plotted to guide the eyes for the high-spin (HS), mixed-spin (MS; HS + LS), and low-spin (LS) regions, respectively (see Supplementary Fig. S2 for details).
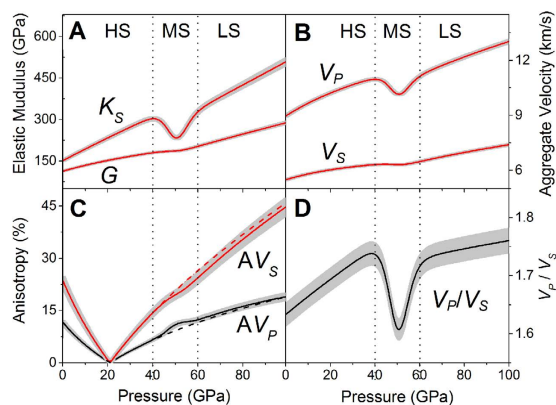
Figure 3. Aggregate bulk and shear moduli K_S and G, aggregate velocities, elastic anisotropies and aggregate V_P/V_S ratio of ferropericlase (Mg$_{0.92}$Fe$_{0.08}$)O at high pressure and 300 K. (**A**) Adiabatic bulk and shear modulus from Voigt-Reuss-Hill average; (**B**) Aggregate compressional V_P and shear wave velocities V_S, where $V_P = \sqrt{K_S + 4/3G/\rho}$ and $V_S = \sqrt{G/\rho}$; (**C**) Compressional and shear wave anisotropy as a function of pressure; dashed lines are the extrapolated anisotropies for the HS state that are plotted for comparison; (**D**) aggregate V_P/V_S ratio. Grey shaded areas represent uncertainties calculated from standard error propagations using the experimentally derived elastic constants. Vertical dashed lines are plotted to guide the eyes for the HS, MS, and LS regions, respectively.

solving Christoffel's equation $\det|C_{ijkl}n_jn_l - \rho V^2\delta_{ik}| = 0$ (Fig. S7). At ambient conditions, the single-crystal ferropericlase exhibits the slowest V_P in the [100] direction and the fastest V_P in the [111] direction, while the V_S is slowest in the [110] direction and fastest in the [100] direction. This anisotropic behavior is reversed at pressures of approximately 21 GPa, above which the V_P minimum and maximum are along the [111] and [100], respectively, while the V_S minimum and maximum are along the [100] and [110] directions. The velocities vary significantly with the propagation direction at pressures above approximately 40 GPa, indicating that single-crystal ferropericlase exhibits strong V_P and V_S anisotropy. The velocity anisotropy factor (A) is defined as $A = (V_{max} - V_{min})/2(V_{max} + V_{min}) \times 100\%$, where V_{max} and V_{min} are the maximum and minimum velocities, respectively[29]. For V_P, the anisotropy is defined as the difference between the maximum and minimum velocities in corresponding propagation directions, while the V_S splitting anisotropy is defined as the velocity difference between the maximum and minimum velocities for two orthogonally polarized V_S velocities along corresponding propagation directions. Our results show that the V_P anisotropy and the V_S splitting anisotropy are 11.5% and 23.5% at ambient conditions, decreasing to almost zero at approximately 21 GPa, and then increasing monotonically up to 40 GPa. The V_P anisotropy increases to ~11% at 50 GPa, which is midway between the spin transition, while the anisotropy of the extrapolated HS state is approximately ~9%. Furthermore, the V_S splitting anisotropy continuously increases with increasing pressure but slightly deviates from the extrapolated HS state counterpart starting with the spin transition (Fig. 3C and Fig. S8). Within the experimental uncertainties in this study, the effect of the spin transition on the V_S splitting anisotropy can be considered negligible (Fig. 3C). Contrary to previous studies[4], our results show that the spin transition is actually associated with a slightly enhanced V_P anisotropy (Fig. S8). Furthermore, our results clearly show that the LS ferropericlase exhibits some unique elastic behavior distinct from that of the HS state, including an enhanced pressure derivative of C_{11}, C_{12}, and C_{44}, implying an enhanced pressure dependence of aggregate K_S, V_P, and G (Figs 2 and 3A,B; Table S2). In particular, the spin transition is associated with a significant reduction of the aggregate V_P/V_S ratio via the aggregate V_P softening since V_S softening does not visibly occur within the spin transition; this ratio is reduced from 1.75 at approximately 40 GPa at the onset of the transition to 1.6 at approximately 50 GPa midway within the transition (Fig. 3B,D). That is, the LS state exhibits a maximum of approximately 12% reduction in the V_P/V_S ratio as compared to that of the extrapolated HS state within the spin transition. Such a reduction in the V_P/V_S ratio manifests an abnormal Poisson's ratio within the spin transition and into the LS state.

Elasticity of ferropericlase along an expected geotherm: implication for lower-mantle seismic heterogeneities. To understand the effects of the spin transition on the elasticity of ferropericlase at relevant P-T conditions of the lower mantle[22,30], we have modelled the elastic constants of ferropericlase along an expected lower-mantle geotherm up to approximately 125 GPa using thermoelastic models and a previously reported spin crossover diagram[23,25]. The geotherm profile at the core-mantle boundary conditions has not been considered in our modelling here. The thermal EoS parameters of ferropericlase with 25 at% iron in a previous experimental report are linearly scaled back for the compositional effects of FeO in MgO to construct the spin crossover diagram for our ferropericlase with 8 at% iron at high P-T (See SI for details). Our modeled results show that the spin crossover of ferropericlase with 8 at% iron occurs between 65 and 105 GPa along the geotherm. The temperature derivatives of the elastic constants for pure MgO[31] are combined with our high-pressure elasticity results (Table S1 and Table S2) to account for the high P-T effects of FeO solid solution for the HS and LS states (Fig. S9). These modelled results show that the effects of the spin crossover on the elastic and seismic parameters along an expected adiabatic geotherm remain profound, even though the spin crossover is broadened by high temperatures (Fig. 4 and Fig. S9). In particular, C_{11} and C_{12} exhibit 15% and 60% maximum reduction, respectively, within the spin crossover at approximately 85 GPa that corresponds to 1900 km in depth. The V_P anisotropy increases to 18.6% at ~85 GPa within the spin transition (a 23% increase in the anisotropy as compared to the extrapolated HS state reference), while the pressure-dependent V_S anisotropy is lower than that of the HS counterpart in the LS state (Fig. S9 B). Compared to the HS state reference, the aggregate V_P decreases by 10% while the V_P/V_S ratio drops by 13% within the spin crossover (Fig. 4). On the other hand, the aggregate V_P and V_S profiles of the LS ferropericlase are significantly higher than that of their HS state counterparts (Fig. 4A). Using the HS state as the reference, we have calculated the deviations of a number of seismic parameters across the spin crossover along an expected mantle geotherm. These results show that the spin crossover produces V_P and V_S velocities and anisotropies, V_P/V_S ratio, and Poisson's ratio that vary as a function of the low-spin fraction as compared to the extrapolated HS state. Specifically, the V_P, V_P/V_S ratio, and Poisson's ratio are significantly reduced within the spin crossover, whereas the LS state exhibits enhanced V_P and V_S velocities as well as reduced V_P/V_S and Poisson's ratio (Fig. S10).

Our modelled velocity profiles show that the V_P profile of ferropericlase with 8 at% iron is significantly reduced by a maximum of 10% within the spin crossover at approximately 1900 km in depth along an expected mantle geotherm, while the V_S profile is slightly enhanced with increasing fraction of the LS state as compared to the extrapolated HS state (Fig. 4). That is, the V_P/V_S ratio is also significantly reduced with the spin crossover. On the other hand, the V_P and V_S profiles of the LS ferropericlase are higher than those of the extrapolated HS state as well as the PREM model toward the lower parts of
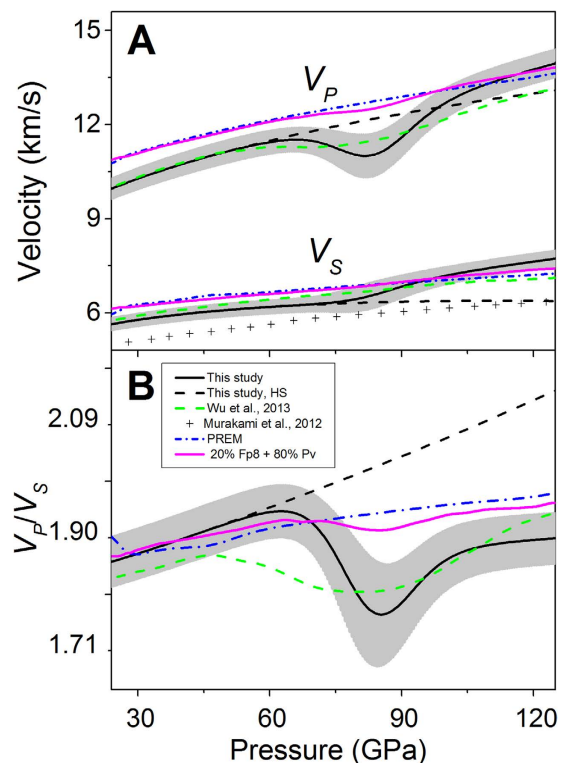
Figure 4. Modelled seismic velocities and V_P/V_S ratio of ferropericlase $((Mg_{0.92}Fe_{0.08})O)$ along an expected lower-mantle geotherm. (**A**) Aggregate compressional and shear wave velocities. These results are calculated from the single-crystal elastic constants. (**B**) Calculated V_P/V_S ratio. Solid lines: modelled seismic parameters with uncertainties shown as grey areas; black dashed lines: modelled parameters for the high-spin state; green dotted lines: theoretical V_P and V_S values of ferropericlase $((Mg_{0.875}Fe_{0.125})O)$[25]; crosses: experimental results with 17% iron[14]. PREM seismic parameters are plotted as blue dotted dashed lines for comparison[6]; The magenta lines are the modelled velocity profiles assuming that the lower mantle is composed of 20% ferropericlase (fp8) and 80% bridgmanite (Pv)[14].

the lower mantle. Considering that ferropericlase in the lower mantle may contain approximately 20% FeO and account for approximately 20 vol.% of the lower-mantle in a pyrolite model[9], our calculated V_P and V_S profiles with 20 vol.% of ferropericlase and 80 vol.% of bridgmanite are fairly consistent with the PREM model at depths from uppermost to mid lower-mantle. On the other hand, the spin crossover in ferropericlase is expected to contribute a few percent reduction in V_P and V_P/V_S ratio in the middle parts of the lower mantle compared to the PREM seismic model, while the occurrence of the LS ferropericlase would result in enhanced V_P and V_S profiles compared to the seismic model (Fig. 4). Since the V_P and V_S velocities of ferropericlase behave quite distinctly across the spin transition, our results here also indicate V_P/V_S ratio can be used as a more sensitive seismic indicator for probing the spin transition-induced heterogeneities in the lower mantle (Figs 3 and 4).

Based on V_S profiles of polycrystalline ferropericlase and bridgmanite at high *P-T* conditions, it has been proposed that the lower mantle is predominantly made of bridgmanite by 93% in volume, called the perovskitic lower mantle, and that ferropericlase may only account for 7% of the lower-mantle mineralogy[14]. In this scenario, the contributions of the elastic and seismic anomalies of ferropericlase across the spin crossover would play a much smaller role on the overall seismic profiles of the lower mantle such that the associated effects may become seismically insignificant. In our modelling, we have considered the lower-mantle *P-T* conditions along an expected adiabatic geotherm, but the possibility of having a super-adiabatic lower mantle with a steeper thermal gradient than the adiabatic geotherm model is possible[14]. The relatively higher geotherm would widen the spin crossover leading to smaller velocity anomalies within the spin crossover and slower V_P and V_S profiles of the LS ferropericlase in the lower mantle. It also remains to be seen as to how the changes in the partitioning coefficient of iron between bridgmanite and ferropericlase $(K_D^{Pv-Fp} = (X_{Fe}^{Pv}/X_{Mg}^{Pv})/(X_{Fe}^{Fp}/X_{Mg}^{Fp}))$ across the spin transition can influence the abnormal elasticity in ferropericlase reported here. Previous studies have shown that the K_D^{Pv-Fp} decreases from approximately 0.85 at ~750 km depth to 0.2 at ~1800 km depth in the pyrolitic composition, indicating that Fe^{2+} preferentially partitions into ferropericlase in the middle to lower part of the lower-mantle conditions[32,33]. That is, the iron content of lower mantle minerals can be largely influenced by the change of the iron partitioning associated with the occurrence of the spin transition.

In this case, the spin crossover of ferropericlase can even occur over a wider range of P-T conditions with variable amounts of iron involved, thus spreading seismic and chemical anomalies in ferropericlase that may become too broad to be seismically detectable with our current seismic resolution. Thus far, seismic studies have yet revealed reliable features of the lower mantle that can be associated with the spin transition effects in the region. Future seismic studies of the lower mantle taking the effects of the spin transition as well as temperature and composition parameters into account are needed to decipher the geophysical consequences of the spin transition of ferropericlase in the region. Our results point to potential consequences of the spin transition for seismic heterogeneities in the lower mantle and also highlight a much more complex picture of the elasticity of ferropericlase in the lower mantle, affecting our understanding of seismology, geochemistry, and geodynamics in the region.

Methods

Single-crystal ferropericlase (($Mg_{0.92}$,$Fe_{0.08}$)O) was synthesized via inter-diffusion of Fe and Mg between a single-crystal periclase and pre-synthesized (Mg,Fe)O powder in a H_2/CO_2 gas-mixing furnace at the Institute for Study of the Earth's Interior (ISEI) of Okayama University at Misasa. The MgO crystal with a pre-oriented (100) crystallographic plane purchased from the MTI Corporation was cut down to 7 mm in length by 7 mm wide and 0.25 mm thick, and was sandwiched between two layers of compacted poly-crystalline ($Mg_{0.75}Fe_{0.25}$)O powder approximately 1 mm thick each. The starting sample assemblage was then placed in a Pt holder into the furnace operating at 1350 °C and 10^{-2} Pa oxygen fugacity for approximately 2 weeks. The synthesized single-crystal ferropericlase was then extracted and polished for further sample analyses. Electron microprobe and X-ray diffraction analyses of the sample at The University of Texas at Austin showed that the sample was chemically homogeneous with the chemical composition of ($Mg_{0.92}Fe_{0.08}$)O and a unit cell parameter of $a = 4.1996$ (4) Å. The (100)-oriented sample was double polished down to approximately 15 μm thick, and cut into squared platelets 50–80 μm in length for high-pressure DAC experiments. The orientation of the platelet was confirmed by the single-crystal X-ray diffraction patterns at ambient and high pressure (Fig. S1B).

High-pressure X-ray diffraction patterns were collected from the single-crystal sample at room temperature in a DAC at the Sector 13-BMD of the GSECARS of the Advanced Photon Source (APS), Argonne National Lab (ANL) (Fig. S1). A pair of diamond anvils with 200 μm culets were used to pre-indent a rhenium gasket with an initial thickness of 250 μm to approximately 25 GPa (or approximately 25 μm thick). Consequently, a hole of 120 μm was drilled in the pre-indented area and used as the sample chamber. A piece of the platelet 50 μm in length was loaded, together with Au powder as the pressure calibrant and Ne as the pressure medium, in a short symmetric DAC. An incident X-ray beam with a wavelength of 0.3344 Å and focused size of 20 μm (FWHM) in diameter was used for the diffraction experiments (Figs S1 and S2). X-ray diffraction patterns of the sample were collected at pressure intervals of 1–3 GPa up to 91 GPa by a MAR CCD by continuously rotating the DAC around the vertical axis of the sample stage by ±15° (Fig. S2). The unit cell parameters and their uncertainties for the sample were calculated based on four sets of the diffraction peaks corresponding to {200}, {220}, {400}, and {420} equivalent reflections (Fig. S1). The uncertainties of the unit cell parameters are typically in the order of 0.04% and are approximately 0.08% at the highest pressure of 91 GPa, indicating that the sample remained sufficiently high quality for the X-ray diffraction, BLS, and ISS experiments. Analysis of the XRD patterns of the sample also confirmed that the crystal was indeed oriented in the (100) crystallographic plane within approximately ±1° angular uncertainty.

High-pressure BLS and ISS experiments were performed on the single-crystal ferropericlase at up to 96 GPa in a short symmetric DAC in the Mineral Physics Laboratory of The University of Texas at Austin. Ultralow birefringence and microscopically defect-free diamond anvils were selected for these experiments using a petrographic microscope under crossed-polar, because we had observed that the pulsed laser of the ISS system with a 1064 nm wavelength could potentially damage diamond anvils having defects and high strained areas. Similar to the sample preparation in the XRD experiments, a pair of diamond anvils with 200 μm culets was used to pre-indent a rhenium gasket and a hole of 120 μm was drilled and used as the sample chamber. A piece of the platelet 50–70 μm in length was loaded, together with a few ruby spheres as the pressure calibrant and Ne as the pressure medium, in a short symmetric DAC. Two runs were conducted for the BLS and ISS experiments (Table S1). Pressure uncertainties were determined from measured ruby fluorescence spectra before and after the BLS and ISS measurements. BLS spectra of the sample were collected from the (100) platelet along the [100] and [110] crystallographic directions in the transmitted geometry with a pressure interval of 3–5 GPa up to 96 GPa (Figs 1 and 2). The BLS system is equipped with a Coherent Verdi V2 laser operating at 532 nm wavelength and 600 mW laser power, together with a JRS interferometer and an APD detector (Count-10B Photo Counting Module with approximately 5 cps from Laser Components, Inc.). The focused laser beamsize at the sample position was approximately 20 μm in diameter while the scattering angle of the BLS system was set at 48° and calibrated against SiO_2 glass and purified water standards. The data collection time was typically 1 hour at pressures below 50 GPa and 2 hours at higher pressures. Analyses of the Brillouin spectra using OriginPro 9.1 software showed strong V_P and V_S peaks with high signal-to-noise ratios at pressures below 20 GPa, while only the V_S peak of the sample was observed at higher pressures as the V_S peak of the diamond anvils saturated the V_P peak of the sample. The measured V_P and V_S velocities

of the sample at pressures below 20 GPa were used to derive the full elastic constants of the crystal and also to cross check the reliability of the ISS results at lower pressures (see further discussion below).

High-pressure ISS spectra were also collected from the single-crystal sample along the [100] and [110] crystallographic directions up to 96 GPa (Fig. 1). The ISS system is a pump-and-probe technique that is equipped with the pump laser with a 1064 nm wavelength and a pulse width of 15 ps and the probe laser with a 532 nm wavelength. The pump laser from Talisker of the Coherent Company was split into two beams which were then recombined at the sample position with a crossing angle of 20.3° and a beam size of 30 μm. The probe laser was delayed by an Aerotech linear stage as long as 20 ns, while the diffracted ISS signals were collected by a photodiode detector. The data collection time for each ISS spectrum was typically 2 hours. Using MATLAB and OriginPro 9.1 softwares, we implemented the Burg method to analyze the time-domain ISS spectra in order to derive the frequency-domain power spectra and the acoustic wave velocities of the sample at high pressures (Fig. 1). The derived V_P values from ISS measurements are consistent with those from the BLS measurements at pressures below 20 GPa, confirming the calibration and reliability of both techniques. The interfacial waves were also observed in most of the ISS experiments, but their signals were much weaker than that of the longitudinal acoustic waves; in fact, the interfacial waves were too weak to be observed in our analyses in some experiments. Given the uncertainties involved in interpretation of the interfacial wave results from ISS experiments, we have only used the V_P from the ISS measurements and the V_S from the BLS experiments, together with the density results from XRD measurements, to derive full elastic constants of the single-crystal ferropericlase at high pressures.

References

1. Crowhurst, J., Brown, J., Goncharov, A. & Jacobsen, S. Elasticity of (Mg,Fe)O through the spin transition of iron in the lower mantle. *Science* **319**, 451 (2008).
2. Marquardt, H., Speziale, S., Reichmann, H. J., Frost, D. J. & Schilling, F. R. Single-crystal elasticity of (Mg$_{0.9}$Fe$_{0.1}$)O to 81 GPa. *Earth Planet. Sci. Lett.* **287**, 345–352 (2009).
3. Antonangeli, D. *et al.* Spin crossover in ferropericlase at high pressure: A seismologically transparent transition? *Science* **331**, 64 (2011).
4. Marquardt, H. *et al.* Elastic shear anisotropy of ferropericlase in Earth's lower mantle. *Science* **324**, 224 (2009).
5. Lin, J. F., Speziale, S., Mao, Z. & Marquardt, H. Effects of the electronic spin transitions of iron in lower mantle minerals: implications for deep mantle geophysics and geochemistry. *Rev. Geophys.* **51**, 244–275 (2013).
6. Dziewonski, A. M. & Anderson, D. L. Preliminary reference Earth model. *Phys. Earth Planet. Inter.* **25**, 297–356 (1981).
7. Kennett, B., Engdahl, E. & Buland, R. Constraints on seismic velocities in the Earth from traveltimes. *Geophys. J. Int.* **122**, 108–124 (1995).
8. Ritsema, J., Deuss, A., Van Heijst, H. & Woodhouse, J. S40RTS: a degree-40 shear-velocity model for the mantle from new Rayleigh wave dispersion, teleseismic traveltime and normal-mode splitting function measurements. *Geophys. J. Int.* **184**, 1223–1236 (2011).
9. Ringwood, A. E. *Composition and Petrology of the Earth's Mantle.* Vol. 618 (McGraw-Hill New York, 1975).
10. Irifune, T. Absence of an aluminous phase in the upper part of the Earth's lower mantle. *Nature* **370**, 131–133 (1994).
11. Matas, J., Bass, J., Ricard, Y., Mattern, E. & Bukowinski, M. On the bulk composition of the lower mantle: predictions and limitations from generalized inversion of radial seismic profiles. *Geophys. J. Int.* **170**, 764–780 (2007).
12. Karato, S. I. & Karki, B. B. Origin of lateral variation of seismic wave velocities and density in the deep mantle. *J. Geophys. Res-Sol. Ea. (1978–2012)* **106**, 21771–21783 (2001).
13. Kellogg, L. H., Hager, B. H. & van der Hilst, R. D. Compositional stratification in the deep mantle. *Science* **283**, 1881–1884 (1999).
14. Murakami, M., Ohishi, Y., Hirao, N. & Hirose, K. A perovskitic lower mantle inferred from high-pressure, high-temperature sound velocity data. *Nature* **485**, 90–94 (2012).
15. Cammarano, F., Marquardt, H., Speziale, S. & Tackley, P. J. Role of iron-spin transition in ferropericlase on seismic interpretation: A broad thermochemical transition in the mid mantle? *Geophys. Res. Lett.* **37**, L03308 (2010).
16. Murakami, M., Hirose, K., Kawamura, K., Sata, N. & Ohishi, Y. Post-perovskite phase transition in MgSiO$_3$. *Science* **304**, 855 (2004).
17. Wentzcovitch, R. *et al.* Anomalous compressibility of ferropericlase throughout the iron spin cross-over. *Proc. Natl. Acad. Sci. USA* **106**, 8447 (2009).
18. Badro, J. *et al.* Iron partitioning in Earth's mantle: toward a deep lower mantle discontinuity. *Science* **300**, 789–791 (2003).
19. Badro, J. *et al.* Electronic transitions in perovskite: Possible nonconvecting layers in the lower mantle. *Science* **305**, 383–386 (2004).
20. Lin, J. F. *et al.* Spin transition of iron in magnesiowüstite in the Earth's lower mantle. *Nature* **436**, 377–380 (2005).
21. Lin, J. F. *et al.* Electrical conductivity of the lower-mantle ferropericlase across the electronic spin transition. *Geophys. Res. Lett.* **34**, 16305 (2007).
22. Tsuchiya, T., Wentzcovitch, R. M., da Silva, C. R. S. & de Gironcoli, S. Spin transition in magnesiowüstite in Earth's lower mantle. *Phys. Rev. Lett.* **96**, 198501 (2006).
23. Mao, Z., Lin, J. F., Liu, J. & Prakapenka, V. B. Thermal equation of state of lower-mantle ferropericlase across the spin crossover. *Geophys. Res. Lett.* **38**, L23308 (2011).
24. Wu, Z. & Wentzcovitch, R. M. Spin crossover in ferropericlase and velocity heterogeneities in the lower mantle. *Proc. Natl. Acad. Sci. USA* **111**, 10468–10472 (2014).
25. Wu, Z., Justo, J. F. & Wentzcovitch, R. M. Elastic anomalies in a spin-crossover system: ferropericlase at lower mantle conditions. *Phys. Rev. Lett.* **110**, 228501 (2013).
26. Brown, J. & Shankland, T. Thermodynamic parameters in the Earth as determined from seismic profiles. *Geophys. J. Roy. Astr. S.* **66**, 579–596 (1981).
27. Fei, Y. *et al.* Spin transition and equations of state of (Mg, Fe)O solid solutions. *Geophys. Res. Lett.* **34**, L17307 (2007).
28. Birch, F. Finite strain isotherm and velocities for single-crystal and polycrystalline NaCl at high pressures and 300 K. *J. Geophys. Res.* **83**, 1257–1268 (1978).
29. Mainprice, D., Barruol, G. & Ismail, W. B. The seismic anisotropy of the Earth's mantle: from single crystal to polycrystal. *Geoph. Monog., AGU* **117**, 237–264 (2000).
30. Lin, J. F. *et al.* Spin transition zone in Earth's lower mantle. *Science* **317**, 1740 (2007).

31. Karki, B., Wentzcovitch, R., De Gironcoli, S. & Baroni, S. First-principles determination of elastic anisotropy and wave velocities of MgO at lower mantle conditions. *Science* **286,** 1705–1707 (1999).
32. Auzende, A. L. *et al.* Element partitioning between magnesium silicate perovskite and ferropericlase: new insights into bulk lower-mantle geochemistry. *Earth Planet. Sci. Lett.* **269,** 164–174 (2008).
33. Sakai, T. *et al.* Fe-Mg partitioning between perovskite and ferropericlase in the lower mantle. *Am. Mineral.* **94,** 921–925 (2009).

Author Contributions

J.F.L. conceived and designed the research. J.F.L., N.T. and T.O. synthesized the starting sample. J.F.L. and X.T. designed and built the ISS system, and X.T. built the analytical programs for analyzing the ISS data. J.Y., X.T. and J.F.L. collected and analyzed the XRD, BLS, and ISS data. J.Y. conducted thermodynamic modelling. J.F.L. and J.Y. wrote the paper, and all authors were involved in the revision of the manuscript.

Additional Information

Supplementary information accompanies this paper at http://www.nature.com/srep

Competing financial interests: The authors declare no competing financial interests.

How to cite this article: Yang, J. *et al.* Elasticity of Ferropericlase across the Spin Crossover in the Earth's Lower Mantle. *Sci. Rep.* **5,** 17188; doi: 10.1038/srep17188 (2015).

Supplementary Material

Elasticity of Ferropericlase across the Spin Crossover in the Earth's Lower Mantle

Jing Yang[a], Xinyue Tong[a], Jung-Fu Lin[a,b,1], Takuo Okuchi[c], Naotaka Tomioka[c]

[a]Department of Geological Sciences, Jackson School of Geosciences, The University of Texas at Austin, Austin, TX 78712, USA

[b]Center for High Pressure Science and Technology Advanced Research (HPSTAR)

[c]Institute for Study of the Earth's Interior, 827 Yamada, Misasa, Tottori, 682-0193 Japan

Supplementary Text

Modelling the Fraction of the High-Spin and Low-Spin States in Ferropericlase

Following the modelling procedures reported in previous studies[1-3], we have used the pressure-volume[4] relations from our X-ray diffraction measurements to evaluate the fraction of the high-spin (HS) and low-spin (LS) states of iron in ferropericlase $(Mg_{0.92}Fe_{0.08})O$ as a function of pressure and temperature (P-T) (Figs. S1 and S2). The P-V data of the ferropericlase was initially compared with the P-V relation of the end-member MgO as a starting reference at high pressures and room temperature[4]. The comparison permits us to clearly evaluate the volume reduction over the pressure range across the spin transition[2]. Since the HS ferropericlase exhibits a similar equation of state (EoS) behavior to that of MgO, such comparison also helps establish the EoS parameters for the HS state[2]. With the width of the transition and the thermal EoS parameters of the HS state initially established, the fraction of the LS state (n_{LS}) at a given P-T condition can be obtained using the following equations[1,3] (Fig. S2):

$$n_{LS} = \frac{1}{1 + \exp\left(\frac{\Delta G(P,T)^*}{T}\right)} \tag{1}$$

$$\Delta G(P,T)^* = b_0(T) + b_1(T)P_n \tag{2}$$

$$P_n = \frac{P - P_{HS}}{P_{LS} - P_{HS}} \tag{3}$$

where $\Delta G(P,T)^*$ is the difference in Gibbs free energy between the LS and HS states, P_n is the normalized pressure as determined by the ending pressure of the HS state (P_{HS}) and the onset pressure of the LS state (P_{LS}), and b_0 and b_1 are two temperature-dependent constants. Using the non-linear least squares fit of the n_{LS} to the P-V data at 300 K, we have obtained $b_0 = 1220$ (25) and $b_1 = -2341$ (46).

Based on the solid-solution mixing of the HS and LS states in the ferropericlase lattice as well as the derived LS fraction (n_{LS}), the unit cell volume of ferropericlase (V) across the spin transition is expressed as the ratio between the unit cell volume of the HS state (V_{HS}) and the LS state (V_{LS}) at a given pressure and 300 K (Fig. S2)[3]:

$$V = (1 - n_{LS})V_{HS} + nV_{LS} \qquad [4]$$

It follows that the isothermal bulk modulus (K_T) of the system across the spin transition can be described using the ratio of the HS and LS states[3]:

$$\frac{V}{K_T} = n_{LS}\frac{V_{LS}}{K_{LS}} + (1 - n_{LS})\frac{V_{HS}}{K_{HS}} - (V_{LS} - V_{HS})\left(\frac{\partial n_{LS}}{\partial P}\right)_T \qquad [5]$$

$$V_{\emptyset} = \sqrt{\frac{K_T}{\rho}} \qquad [6]$$

where K_{HS} and K_{LS} are the K_T of the HS and LS state, respectively, ρ is the density, and V_{Φ} is the bulk sound velocity (Figs. S2 and S3).

Derivation of the Full Elastic Constants of the Single-Crystal Ferropericlase

The ferropericlase platelet with (100) orientation allows us to measure V_P velocities as well as V_S velocities with <110> polarization along principle [100] and [110] crystallographic axes using the ISS and BLS techniques, respectively, in a DAC. Together with the *P-V* data from synchrotron X-ray diffraction measurements (Figs. S1 and S2), here we have combined the V_S data from BLS measurements and the V_P data from ISS measurements (Fig. 1) to derive the elastic constants (C_{11}, C_{12}, C_{44}) of the single-crystal ferropericlase using the following equations[5] (Fig. 2 and Fig. S6):

$$V_P [100] = (C_{11}/\rho)^{1/2} \qquad [7]$$

$$V_S [100] < 110 >= (C_{44}/\rho)^{1/2} \qquad [8]$$

$$V_P [110] = [(C_{11} + C_{12} + 2C_{44})/2\rho]^{1/2} \qquad [9]$$

$$V_S [110] < 110 >= [(C_{11} - C_{12})/2\rho]^{1/2} \qquad [10]$$

where [uvw] represents the crystallographic direction for the acoustic wave propagation, and <uvw> indicates the polarization direction. Since the method for deriving the full elastic constants involves multiple experimental data sets and the use of multiple equations listed above, the elastic constants reported here are derived from internally-consistent numerical iterations through minimization of the uncertainties in the derived parameters using the aforementioned equations as well as the finite-strain equations discussed below[6]. In the finite-strain modelling, the pressure derivatives of K_S and G at a given temperature (($\partial K_S/\partial P)_T$ and $(\partial G/\partial P)_T$) are obtained by fitting the moduli at high pressure using the third-order Eulerian finite-strain equation of state (EoS)[7]:

$$K_S = K_{S0}(1 + 2f)^{5/2}\{1 + [3(\partial K_S/\partial P)_T - 5]f\} \qquad [11]$$

$$G = (1 + 2f)^{5/2}\{G_0 + [3(\partial G/\partial P)_T K_{S0} - 5G_0]f\} \qquad [12]$$

$$f = \left(\frac{1}{2}\right)[(V_0/V)^{\frac{2}{3}} - 1] \qquad [13]$$

where f is the Eulerian strain, and V_0 and V are the unit-cell volumes at ambient conditions and high pressures, respectively. The derived K_S and $(\partial K_S/\partial P)_T$ are converted to the isotherm bulk modulus (K_T) and its pressure derivative at constant temperature (($\partial K_T/\partial P)_T$) using the following thermodynamic relations[8]:

$$K_{T0} = K_{S0}/(1 + \alpha\gamma T) \qquad [14]$$

$$(\partial K_T/\partial P)_T = (1 + \alpha\gamma T)^{-1}[\left(\frac{\partial K_S}{\partial P}\right)_T - (\frac{\gamma T}{K_{T0}})(\partial K_T/\partial T)_P] \qquad [15]$$

where $(\partial K_T/\partial T)_P$ is the temperature derivative of the K_T at constant pressure, K_{T0} is the isothermal bulk modulus at ambient conditions, α is the thermal expansion coefficient, and γ is the Grüneisen parameter. Literature values for these parameters $((\partial K_T/\partial T)_P = -0.017$ GPa K^{-1}, $\alpha = 3.76{\times}10^{-5}$ K^{-1}, and $\gamma = 1.443$) are used for the conversion[2,4]. The aforementioned procedures were iterated numerically until both K_T and $(\partial K_T/\partial P)_T$ values were self-consistent with the P-V data. The derived K_T and $(\partial K_T/\partial P)_T$ values were then used to construct the isothermal EoS of the ferropericlase at high P-T.

We have also followed procedure reported in the literature to model the C_{ij} of ferropericlase across the spin transition as a function of pressure[9]. Initially, the Eulerian finite-strain theory is applied to model the C_{ij} of the HS state up to 40 GPa and the LS state above 60 GPa, respectively, at ambient temperature. These elastic constants and their pressure derivatives for the HS and LS states are then used to evaluate the C_{ij} of the mixed-spin (MS) state using the derived n_{LS} and thermoelastic equations described below in which the elastic compliances, S_{ij}, at a given P-T condition are defined as[9]:

$$S^{ij} = -\frac{1}{V}\frac{\partial^2 G}{\partial\sigma_i\partial\sigma_j}|_{P,T} \qquad [16]$$

where G is the total Gibbs free energy of the system, and σ_i and σ_j are the i_{th} and j_{th} stress components, respectively, in the Voigt notation. The elastic compliances for the cubic ferropericlase are given as[9]:

$$S^{11}V = nS_{LS}^{11}V_{LS} + (1-n)S_{HS}^{11}V_{HS} - 1/9(V_{LS}-V_{HS})\frac{\partial n}{\partial P} \qquad [17]$$

$$S^{12}V = nS_{LS}^{12}V_{LS} + (1-n)S_{HS}^{12}V_{HS} - 1/9(V_{LS}-V_{HS})\frac{\partial n}{\partial P} \qquad [18]$$

$$S^{44}V = nS_{LS}^{44}V_{LS} + (1-n)S_{HS}^{44}V_{HS} \qquad [19]$$

The relationships between the elastic constants and the compliances are described as[10]:

$$C_{11} = \frac{S^{11} + S^{12}}{(S^{11} - S^{12})(S^{11} + 2S^{12})} \tag{20}$$

$$C_{12} = \frac{-S^{12}}{(S^{11} - S^{12})(S^{11} + 2S^{12})} \tag{21}$$

$$C_{44} = \frac{1}{S^{44}} \tag{22}$$

Comparison of the modelled elastic constants with experimental results shows a good agreement with each other in the HS, MS, and LS states, validating the thermoelastic theory for the elasticity of ferropericlase across the spin transition[9] (Fig. 2).

Comparison of the Velocity Results at High Pressures

Here we compare our results with the ones reported in previous studies using similar BLS and ISS techniques. Our measured V_S values along [100] and [110] directions are mostly consistent with those in previous BLS measurements for ferropericlase with 10 at.% iron for the high-spin state [11], but are slightly higher within the spin transition and in the low-spin state (Fig. S5). The difference within the spin transition can be explained as a result of different iron contents in these measurements as higher iron content is expected to contribute to a stronger effect on the velocity. Comparison of our measured V_P with previous BLS measurements below 20 GPa shows great consistency within uncertainties[12], whereas there is a significant discrepancy within the spin transition and in the low-spin state (Fig. S5). Our present results show a stronger V_P softening within the spin transition and a lower V_P in the low spin state than that in the previous ISS measurements for ferropericlase with 6% iron. These differences may be explained by the different iron contents, pressure media, as well as experimental uncertainties including the orientation of the crystal used in the experiments.

**Modelling Thermoelastic Parameters across the Spin Crossover in the Lower Mantle**

Using the experimentally-derived thermal EoS parameters and the elastic constants at high pressures and 300 K, we have further modelled the elasticity of ferropericlase (($Mg_{0.92}Fe_{0.08}$)O) at high P-T conditions relevant to the lower mantle along an expected geotherm[13] (Fig. 4 and Fig. S9). Literature results for the spin crossover of ferropericlase (($Mg_{0.75}Fe_{0.25}$)O) are used to construct the spin crossover diagram for our ferropericlase with 8 at.% iron. To reconstruct the spin crossover diagram for our sample, the spin transition pressure of 40-60 GPa at 300 K is used for our ferropericlase sample, instead of 50-75 GPa for ferropericlase with 25 at.% Fe content[2]. Based on previous studies[1,14], elevated temperature widens the spin crossover toward higher pressures. Assuming the thermoelastic properties of ferropericlase can be scaled linearly as a function of the iron concentration, the parameters b_0 and b_1 in the equation (2) can be derived from the non-linear least squares fit to the derived n_{LS} as a function of P-T:

$$b_0 = -262.5 + 4.9T - 3.0 \times 10^{-4}T^2 \qquad [23]$$

$$b_1 = 3155.1 - 16.4T - 8.5 \times 10^{-4}T^2 \qquad [24]$$

Together with the literature values for the thermal expansion coefficient of ferropericlase in the HS and LS state (α_{HS} and α_{LS})[2] and the temperature derivative of the elastic constants[15], we have used the modelled spin crossover diagram and the elastic compliances at high pressures and 300 K to calculate the elastic constants at high P-T using MATLAB (Fig. 4 and Fig. S9)[9].
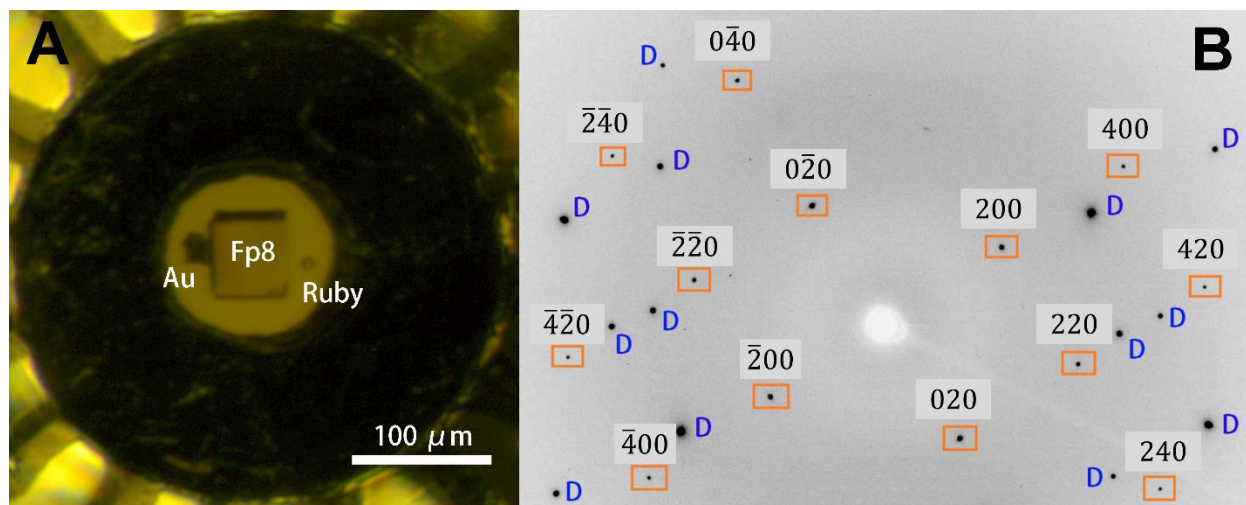
Fig. S1. Representative sample image and X-ray diffraction pattern of the single-crystal ferropericlase $(Mg_{0.92}Fe_{0.08})O$ at high pressure. (A) Ferropericlase (100) platelet, together with Au and a ruby sphere calibrant[16], loaded into a diamond anvil cell having Ne pressure medium at 13 GPa; (B) Representative X-ray diffraction pattern of the single-crystal ferropericlase at 13 GPa. The diffraction pattern was taken by rotating the diamond cell $\pm 15°$ about the vertical axis of the sample stage. D: diffraction spots from the diamond anvil.
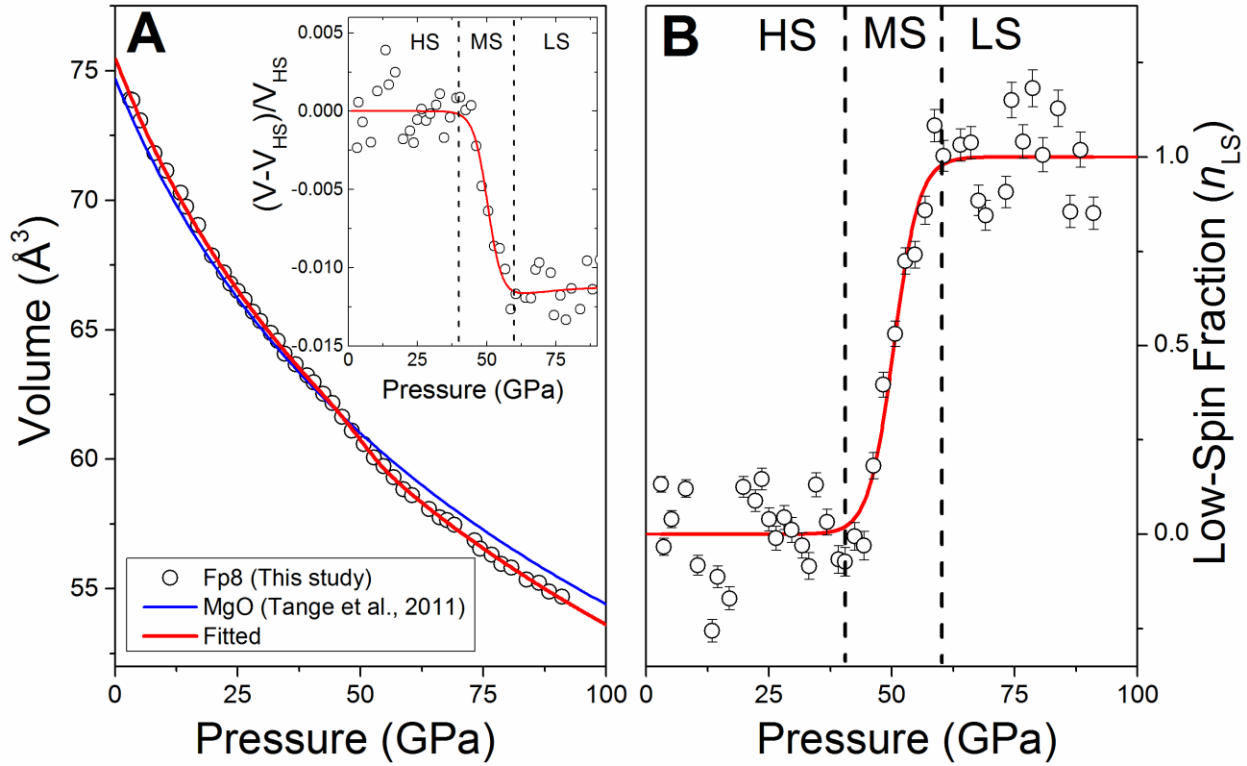
Fig. S2. Pressure-volume relation and the derived low-spin fraction of iron in the single-crystal ferropericlase $(Mg_{0.92}Fe_{0.08})O$ at high pressures. (A) Pressure-volume relation of ferropericlase. Open circles: unit cell volumes as a function of pressure from experimental X-ray diffraction measurements at 300 K; red line: Birch-Murnaghan EoS fit to the experimental data; blue line: pressure-volume curve of the end-member MgO plotted for comparison[4]. The inserted figure shows the volume reduction across the spin transition using the EoS of the high-spin ferropericlase as the reference[2]; (B) Modelled low-spin fraction of the ferropericlase as a function of pressure. The experimental data (open circles) are modelled to derive the low-spin fraction (red line) based on the procedures reported previously[1,2,17]. Vertical dashed lines are plotted to guide the eyes for the high-spin (HS), mixed-spin (MS), and low-spin (LS) regions, respectively.
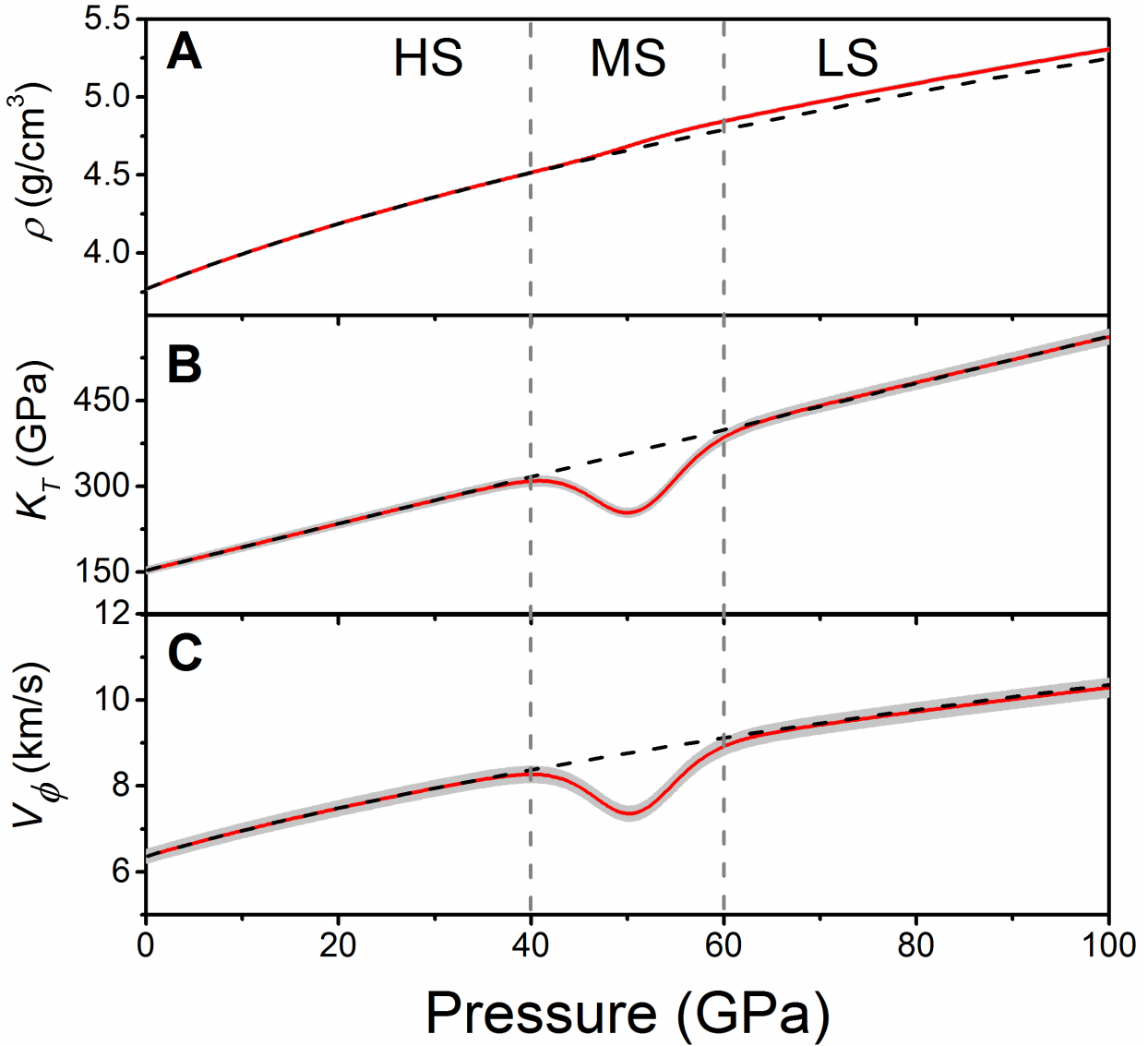
Fig. S3. Equation of state parameters of the single-crystal ferropericlase $(Mg_{0.92}Fe_{0.08})O$ at high pressures and 300 K. (A) Density (ρ); (B) Isotherm bulk modulus (K_T); (C) Bulk sound velocity (V_Φ). Red solid lines: modelled EoS parameters across the spin transition; dash lines: extrapolated EoS parameters for the HS ferropericlase. Grey shaded areas show the uncertainties of the parameters calculated from standard error propagations. Error bars (grey shaded areas) for the density are too small to be shown in the figure.
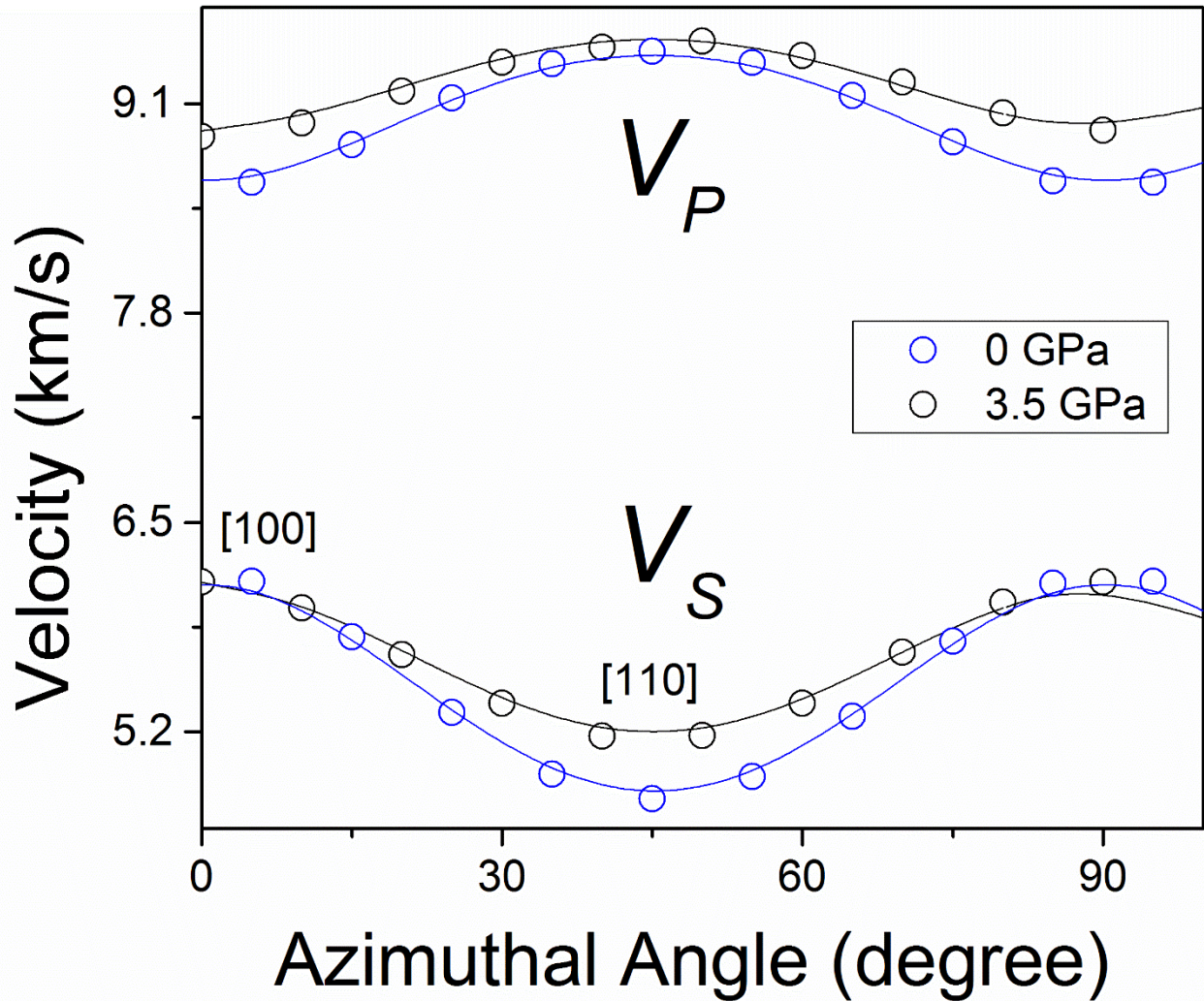
Fig. S4. Compressional (V_P) and shear (V_S) wave velocities of ferropericlase in the (100) platelet as a function of azimuthal angle at ambient conditions (blue circles) and 3.5 GPa (black circles). Uncertainties of the velocities are smaller than the size of the symbols and are not shown for clarity. Solid lines represent modelled velocity profiles from the best fit to the single-crystal elastic constants for each given pressure. These orientation-dependent measurements also help use to locate the [100] and [110] directions for the (100) platelet.
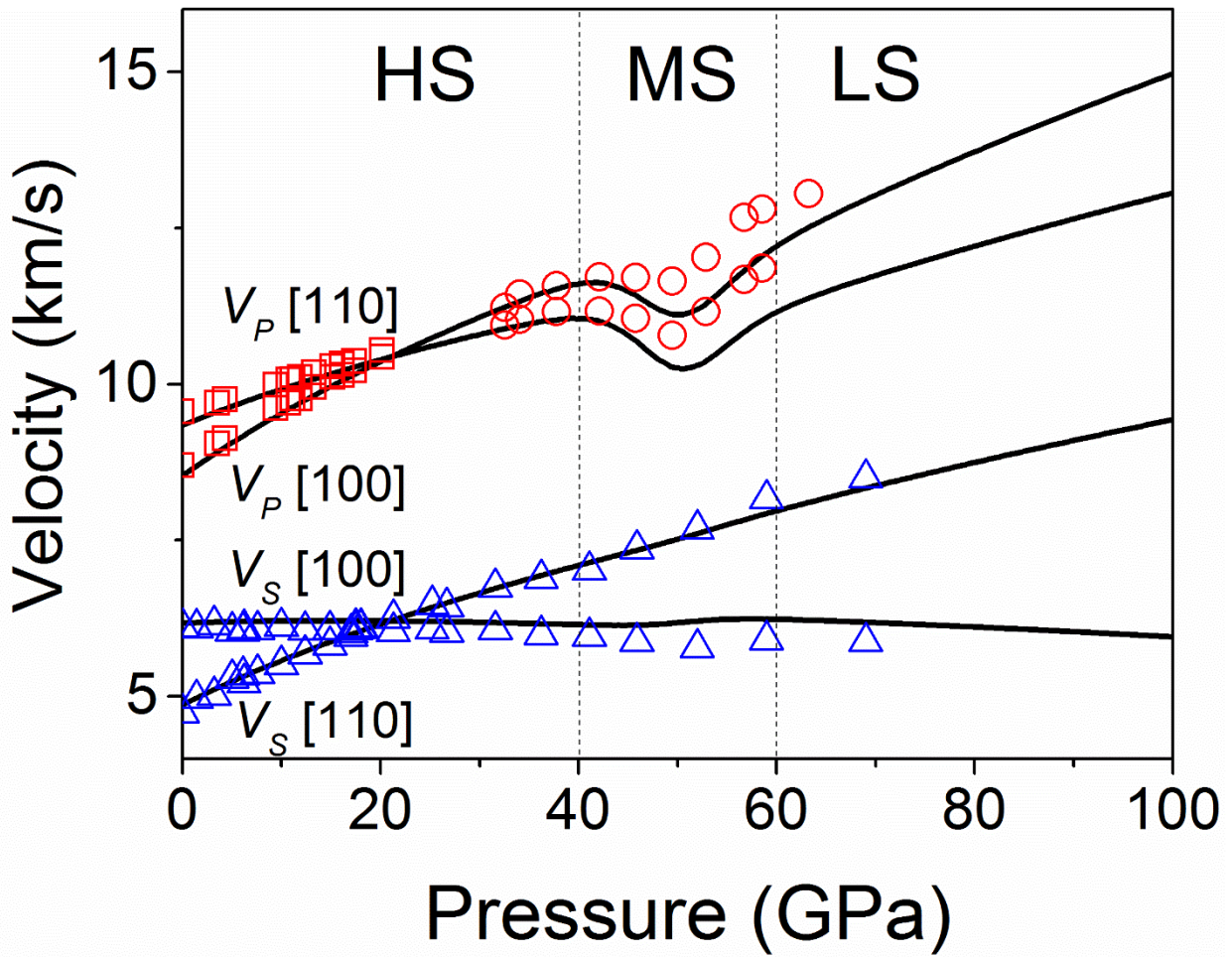
Fig. S5. Comparison of our results with previously reported velocities of ferropericlase at high pressures. Solid lines are modelled experimental results in this study; red squares are BLS measurement for $X_{Fe} = 0.06$ up to 20 GPa[12]; red circles are ISS measurement for $X_{Fe} = 0.06$ up to 60 GPa[18]; blue triangles are BLS measurement for $X_{Fe} = 0.1$ up to 70 GPa[11].
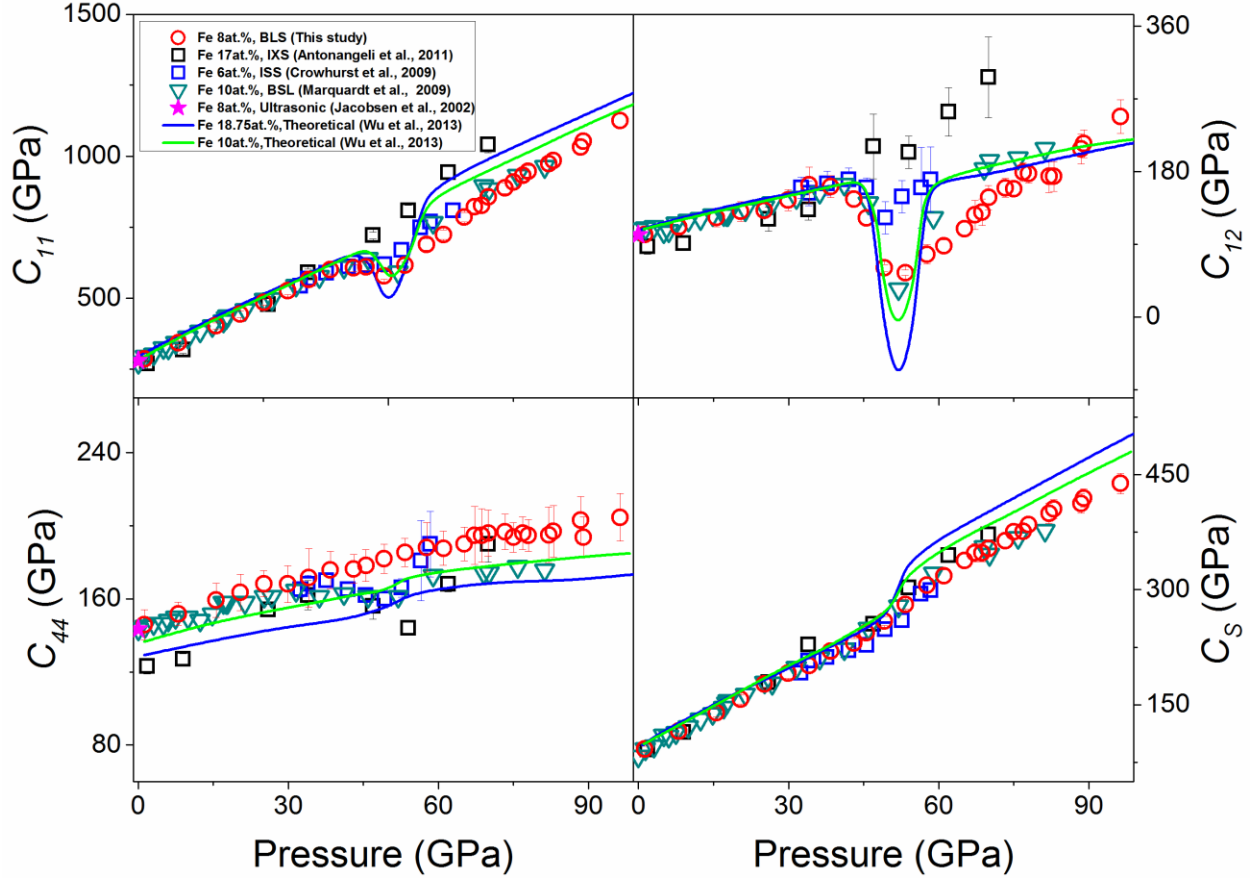
Fig. S6. Comparison of the elastic constants of ferropericlase as a function of pressure. C_S is defined as $(C_{11}-C_{12})/2$. Red circles: combined BLS and ISS measurements with 8% iron in this study; black squares: IXS study with 17% iron content[19]; green circles: BLS study below 20 GPa with 6% iron content[12]; blue triangles: ISS measurements with 6% iron[18]; dark cyan down triangles: BLS study with 10% iron[11]; magenta stars: ultrasonic measurements with 8% iron[20]; blue and green lines: theoretical results with 18.75% and 10% iron content, respectively[9].
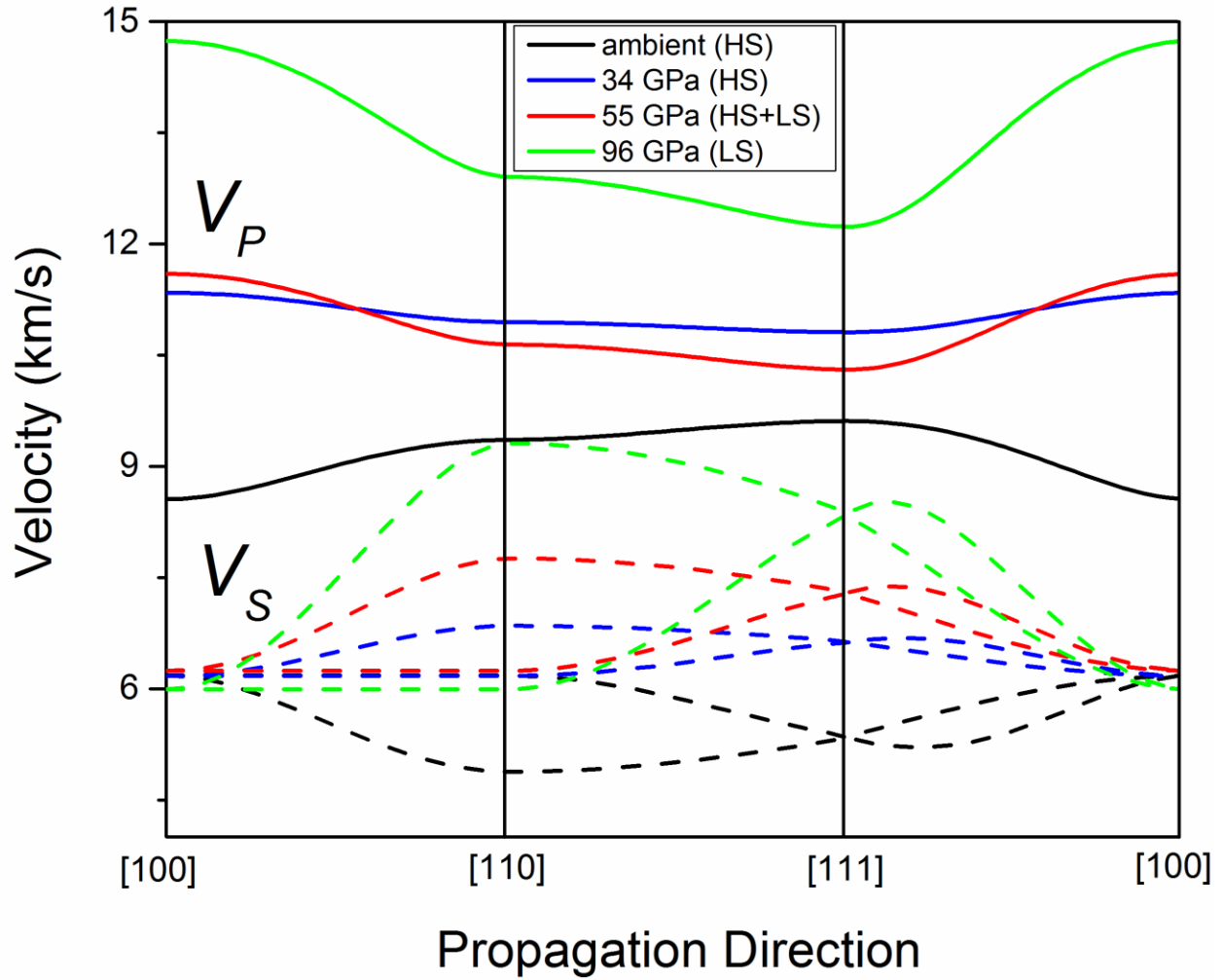
Fig. S7. Compressional (V_P) and shear (V_S) wave velocities of the single-crystal ferropericlase (Mg$_{0.92}$Fe$_{0.08}$)O as a function of the propagation direction at high pressures. The velocities at representative pressures are plotted to highlight the changes in compressional and shear wave anisotropies across the spin transition.
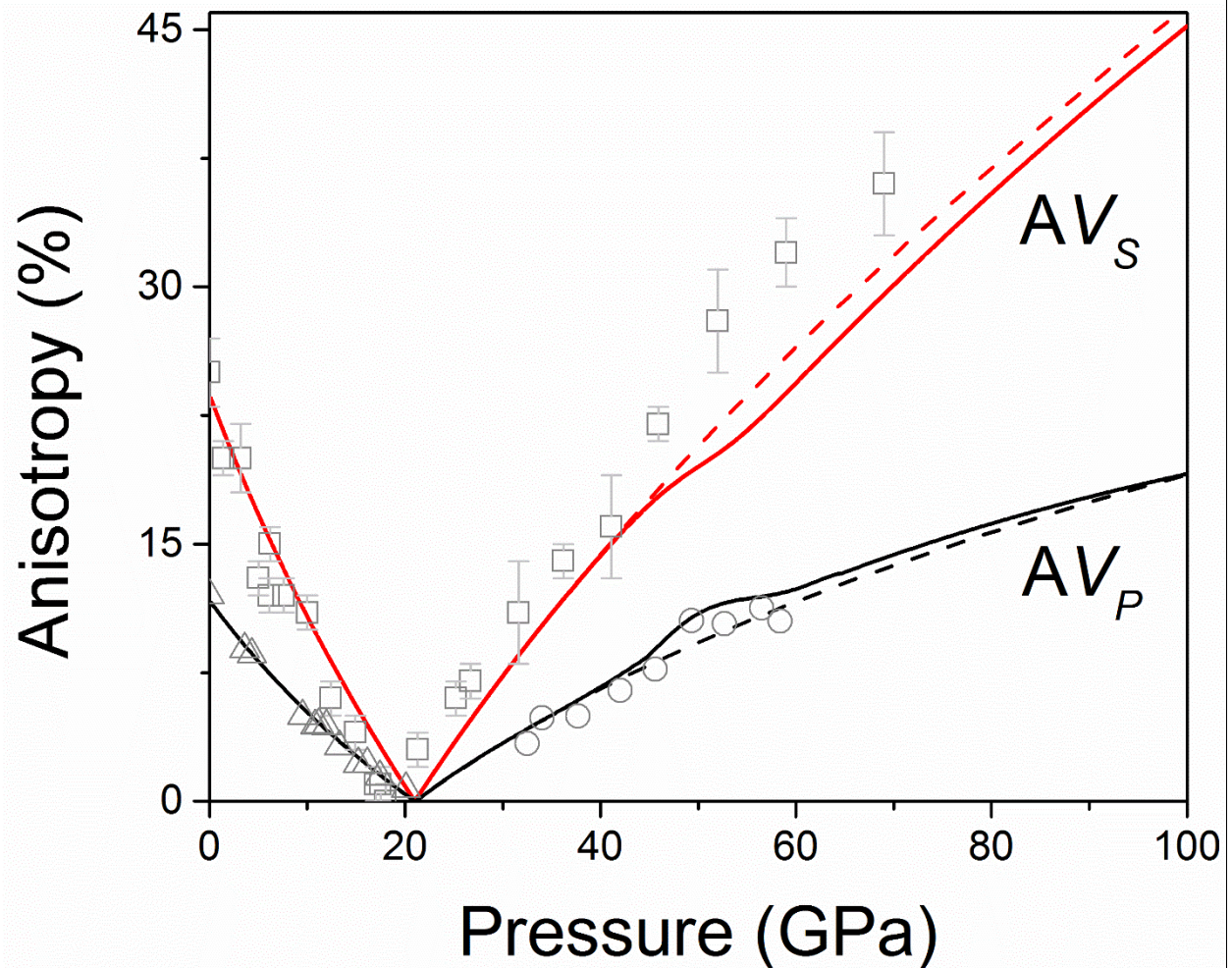
Fig. S8. Compressional and shear wave anisotropy as a function of pressure at 300 K. Red lines: shear wave anisotropy; black lines: compressional wave anisotropy. Dashed lines are the extrapolated anisotropies for the HS state that are plotted for comparison. Open squares: shear wave anisotropy calculated from directly measured velocities along [100] and [110] using equation $(V_S [100] - V_S [110]) / (V_S [100] + V_S [110])/2$ via BLS measurement[11]; open triangles: compressional wave anisotropy calculated from elastic constants measured by BLS using Christoffel's equations[12]; open circles: compressional wave anisotropy calculated from elastic constants measured by ISS using Christoffel's equations[18] .
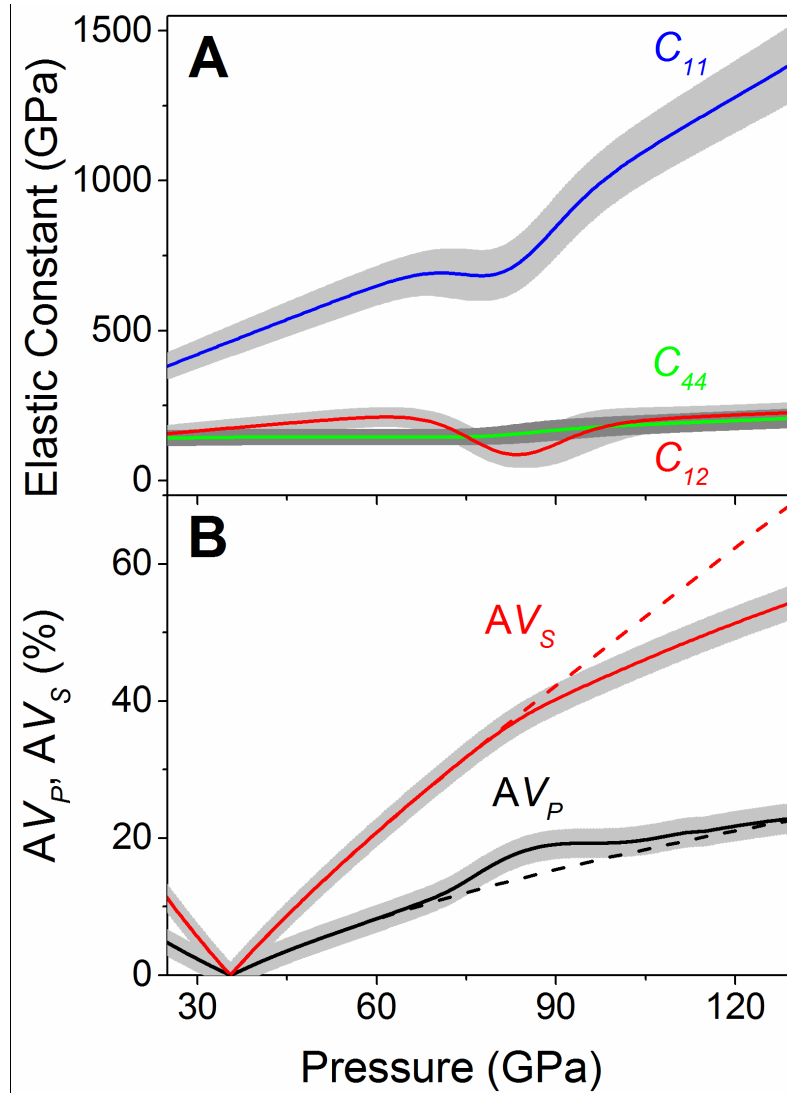
Fig. S9. Modelled elastic properties of ferropericlase $(Mg_{0.92}Fe_{0.08})O$ across the spin transition zone along an expected lower-mantle geotherm. (A) Elastic constants: C_{11}, C_{12}, and C_{44} plotted as blue, red, and green lines, respectively. (B) V_P and V_S anisotropy. Red line: V_S anisotropy; black line: V_P anisotropy. The V_P and V_S anisotropies are calculated using the equations $AV_P = (V_P max - V_P min)/2(V_P max + V_P min)$ and $AV_S = (V_S max - V_S min)/2(V_S max + V_S min)$, where subscripted *min* and *max* represent the minimum and maximum velocity of the single crystal,

respectively. Grey shaded areas show the uncertainties calculated using standard error propagations.
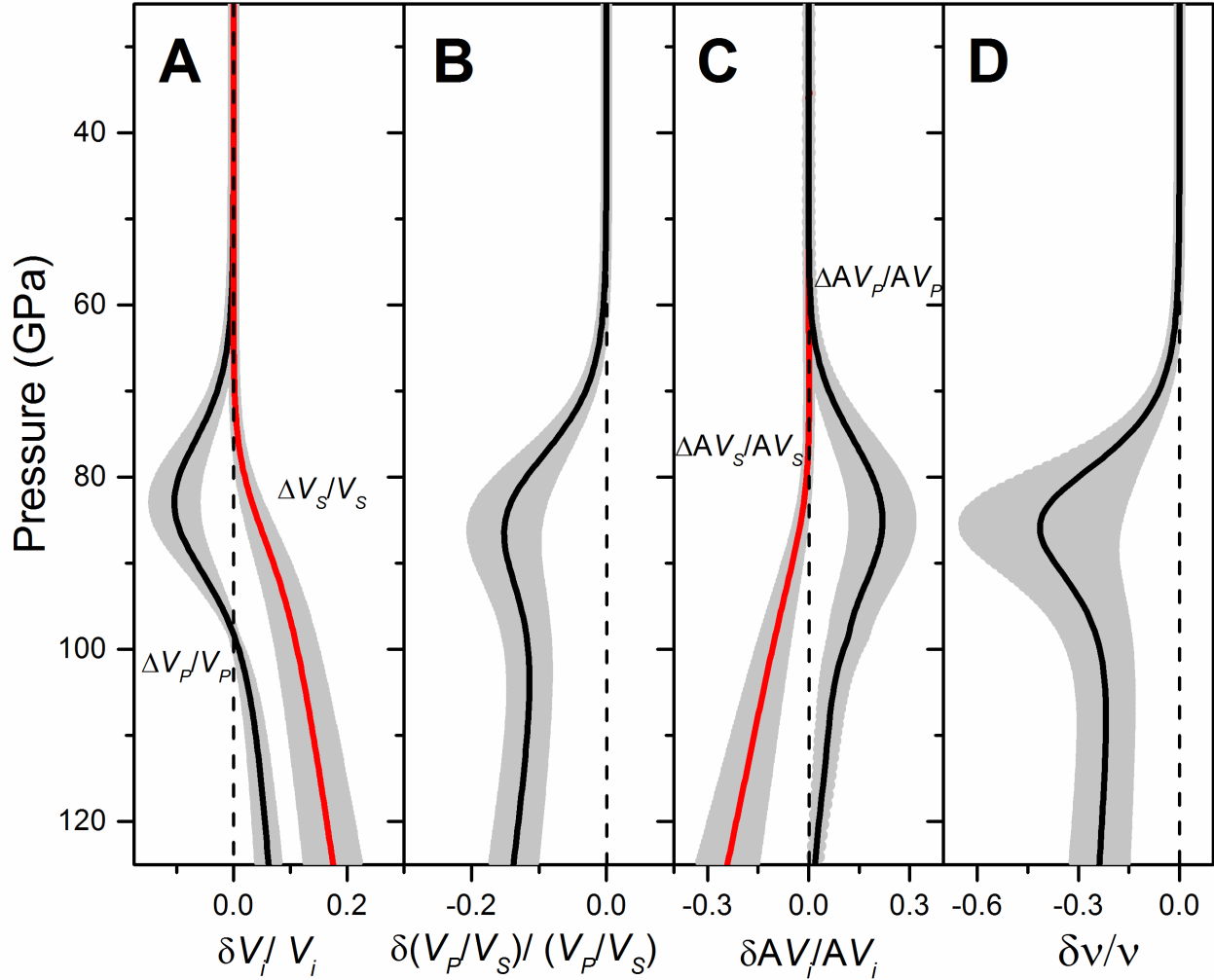
Fig. S10. Variations of the seismic parameters of ferropericlase $(Mg_{0.92}Fe_{0.08})O$ as a function of depth along an expected lower-mantle geotherm. The variations were derived using the modelled seismic parameters of the high-spin ferropericlase as the reference. (A) Aggregate V_P and V_S; (B) V_P/V_S ratio; (C) V_P and V_S anisotropy; (D) Poisson's ratio.

Table S1. Experimental results for ferropericlase $(Mg_{0.92}Fe_{0.08})O$. V_P velocities were derived from ISS measurements while V_S velocities were from BLS measurements.

Pressure	Density g/cm^3	V_P [100] km/s	V_P [110] km/s	V_S [100] km/s	V_S [110] km/s	C_{11} GPa	C_{12} GPa	C_{44} GPa
Run 1								
1.3(0.1)	3.80	8.61(0.08)	9.52(0.09)	6.14(0.07)	4.97(0.06)	287(8)	102(9)	146(8)
8.0(0.1)	3.95	9.21(0.08)	9.87(0.09)	6.12(0.07)	5.46(0.07)	343(8)	112(7)	152(6)
15.6(0.2)	4.11	9.83(0.10)	10.19(0.09)	6.17(0.07)	5.87(0.07)	403(11)	123(11)	159(9)
20.4(0.0)	4.20	10.23(0.07)	10.42(0.06)	6.19(0.10)	6.15(0.06)	445(12)	131(12)	163(10)
25.2(0.3)	4.28	10.56(0.07)	10.64(0.07)	6.19(0.10)	6.47(0.07)	486(10)	132(8)	168(7)
29.9(0.5)	4.36	10.93(0.06)	10.81(0.07)	6.15(0.10)	6.65(0.07)	527(14)	144(13)	168(10)
34.2(0.6)	4.43	11.29(0.07)	11.02(0.07)	6.21(0.10)	6.75(0.09)	566(20)	164(22)	172(16)
38.5(0.8)	4.49	11.50(0.09)	11.19(0.09)	6.19(0.10)	7.03(0.10)	601(15)	161(14)	176(10)
43.1(0.9)	4.56	11.43(0.15)	11.08(0.07)	6.12(0.22)	7.15(0.10)	607(13)	146(10)	176(8)
45.6(1.0)	4.60	11.43(0.12)	10.94(0.07)	6.15(0.20)	7.31(0.10)	610(14)	122(9)	178(9)
49.2(1.2)	4.67	11.05(0.08)	10.44(0.07)	6.16(0.20)	7.49(0.11)	579(12)	61(4)	182(8)
53.3(1.1)	4.28	11.30(0.07)	10.55(0.06)	6.17(0.20)	7.72(0.11)	616(12)	55(3)	176(8)
57.7(1.2)	4.81	11.84(0.10)	11.01(0.08)	6.13(0.10)	8.02(0.11)	689(19)	78(12)	188(14)
61.0(1.5)	4.86	12.11(0.08)	11.14(0.06)	6.12(0.15)	8.13(0.18)	724(16)	88(7)	188(9)
65.2(1.0)	4.91	12.57(0.08)	11.46(0.07)	6.14(0.15)	8.33(0.11)	786(17)	109(8)	190(9)
67.3(0.4)	4.94	12.77(0.13)	11.76(0.17)	6.14(0.11)	8.45(0.20)	823(24)	127(18)	195(16)
70.0(2.0)	4.97	13.00(0.12)	11.95(0.14)	6.16(0.11)	8.49(0.10)	856(22)	148(15)	196(13)
75.0(2.0)	5.03	13.36(0.19)	12.10(0.19)	6.11(0.11)	8.67(0.10)	909(18)	159(10)	194(8)
78.0(2.0)	5.06	13.58(0.20)	12.30(0.23)	6.10(0.11)	8.75(0.21)	947(20)	177(11)	195(9)
83.0(2.0)	5.12	13.74(0.10)	12.41(0.30)	6.06(0.11)	8.94(0.21)	985(26)	174(18)	197(14)
89.0(2.0)	5.19	14.17(0.28)	12.69(0.40)	6.03(0.11)	9.02(0.11)	1053(24)	215(17)	194(11)
Run 2								
68.7(1.3)	4.95	12.78(0.13)	11.76(0.07)	6.13(0.10)	8.43(0.10)	826(23)	130(17)	195(15)
73.3(1.5)	5.01	13.21(0.10)	12.07(0.17)	6.16(0.10)	8.56(0.14)	888(19)	160(12)	197(10)
76.9(1.1)	5.05	13.49(0.10)	12.28(0.20)	6.12(0.10)	8.67(0.15)	932(19)	179(12)	196(9)
82.1(1.6)	5.11	13.75(0.21)	12.30(0.30)	6.13(0.10)	8.86(0.10)	973(27)	174(20)	195(15)
88.5(1.1)	5.18	14.00(0.25)	12.70(0.20)	6.13(0.10)	8.96(0.10)	1033(25)	208(19)	203(13)
96.4(1.7)	5.27	14.50(0.28)	13.10(0.20)	6.10(0.15)	9.17(0.16)	1125(27)	248(21)	205(13)

Table S2. Elasticity of ferropericlase $(Mg_{0.92}Fe_{0.08})O$ in the high-spin and low-spin state at 300 K.

	$(\partial C_{11}/\partial P)_T$	$(\partial C_{12}/\partial P)_T$	$(\partial C_{44}/\partial P)_T$
HS	8.99 (0.1)	1.95(0.12)	1.22(0.10)
LS	9.9 (0.2)	2.2(0.2)	1.3(0.2)

Supplementary References:

1   Tsuchiya, T., Wentzcovitch, R. M., da Silva, C. R. S. & de Gironcoli, S. Spin transition in magnesiowüstite in Earth's lower mantle. *Phys. Rev. Lett.* **96**, 198501 (2006).

2   Mao, Z., Lin, J. F., Liu, J. & Prakapenka, V. B. Thermal equation of state of lower-mantle ferropericlase across the spin crossover. *Geophys. Res. Lett.* **38**, L23308 (2011).

3   Wentzcovitch, R. *et al.* Anomalous compressibility of ferropericlase throughout the iron spin cross-over. *Proc. Natl. Acad. Sci. USA* **106**, 8447 (2009).

4   Tange, Y., Nishihara, Y. & Tsuchiya, T. Unified analyses for P-V-T equation of state of MgO: A solution for pressure-scale problems in high P-T experiments. *J. Geophys. Res-Sol. Ea. (1978–2012)* **114** (2009).

5   Every, A. General closed-form expressions for acoustic waves in elastically anisotropic solids. *Phys. Rev. B* **22**, 1746 (1980).

6   Yang, J., Mao, Z., Lin, J.-F. & Prakapenka, V. B. Single-crystal elasticity of the deep-mantle magnesite at high pressure and temperature. *Earth Planet. Sci. Lett.* **392**, 292-299 (2014).

7   Birch, F. Finite strain isotherm and velocities for single-crystal and polycrystalline NaCl at high pressures and 300 K. *J. Geophys. Res.* **83**, 1257-1268 (1978).

8   Poirier, J.-P. *Introduction to the Physics of the Earth's Interior*. (Cambridge University Press, 2000).

9   Wu, Z., Justo, J. F. & Wentzcovitch, R. M. Elastic anomalies in a spin-crossover system: ferropericlase at lower mantle conditions. *Phys.Rev.Lett.* **110**, 228501 (2013).

10   Nye, J. F. *Physical properties of crystals: their representation by constants and matrices*. (Oxford university press, 1985).

11   Marquardt, H. *et al.* Elastic shear anisotropy of ferropericlase in Earth's lower mantle. *Science* **324**, 224 (2009).

12   Jackson, J. M. *et al.* Single-crystal elasticity and sound velocities of ($Mg_{0.94}Fe_{0.06}$) O ferropericlase to 20 GPa. *J. Geophys. Res.* **111** (2006).

13   Brown, J. & Shankland, T. Thermodynamic parameters in the Earth as determined from seismic profiles. *Geophys. J. Roy. Astr. S.* **66**, 579-596 (1981).

14   Lin, J. F. *et al.* Spin transition zone in Earth's lower mantle. *Science* **317**, 1740 (2007).

15   Karki, B. B., Stixrude, L. & Wentzcovitch, R. M. High-pressure elastic properties of major materials of Earth's mantle from first principles. *Rev. Geophys.* **39**, 507–534 (2001).

16   Fei, Y. *et al.* Toward an internally consistent pressure scale. *Proc. Natl. Acad. Sci. USA* **104**, 9182-9186 (2007).

17   Speziale, S. *et al.* Iron spin transition in Earth's mantle. *Proc. Natl. Acad. Sci. USA* **102**, 17918 (2005).

18   Crowhurst, J., Brown, J., Goncharov, A. & Jacobsen, S. Elasticity of (Mg,Fe)O through the spin transition of iron in the lower mantle. *Science* **319**, 451 (2008).

19   Antonangeli, D. *et al.* Spin crossover in ferropericlase at high pressure: A seismologically transparent transition? *Science* **331**, 64 (2011).

20   Jacobsen, S. D. *et al.* Structure and elasticity of single-crystal (Mg,Fe)O and a new method of generating shear waves for gigahertz ultrasonic interferometry. *J. Geophys. Res.* **107**, 2037 (2002).